

# Using Ligand Engineering to Produce Efficient and Stable Pb-Sn Perovskite Solar Cells with Antioxidative 2D Capping Layers

*Ge Wang,<sup>†,#</sup> Chen Wang,<sup>†,#</sup> Roderick C. I. MacKenzie,<sup>‡</sup> Zihan Zhu,<sup>†</sup> Yi Chen,<sup>†</sup> Shengping Ruan,<sup>†</sup> and Shanpeng Wen<sup>†,\*</sup>*

<sup>†</sup>College of Electronic Science & Engineering, Jilin University, Changchun 130012, P. R. China.

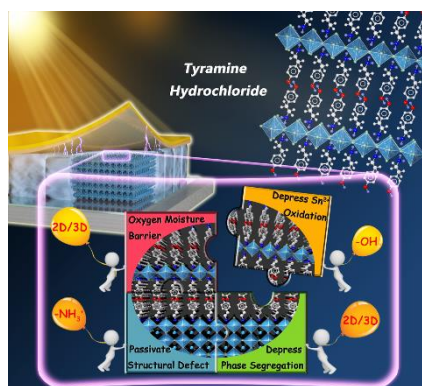
<sup>‡</sup>Faculty of Engineering, University of Nottingham, University Park, Nottingham, NG7 2RD, UK.

Email: [sp\\_wen@jlu.edu.cn](mailto:sp_wen@jlu.edu.cn)

KEYWORDS tyramine hydrochloride, Sn-Pb perovskites, 2-dimensional capping layers, antioxidants, phase segregation

**ABSTRACT** Pb-Sn binary halide perovskites are a promising photovoltaic material due to their low toxicity and optical absorption spectrum well matched to the solar spectrum. However, the ready oxidation of  $\text{Sn}^{2+}$  to  $\text{Sn}^{4+}$  makes the material system currently too unstable to commercialize. Herein, ligand engineering based on anti-oxidative tyramine (hydrochloride, TACl) is presented for the first time to increase the stability of this material system. Using this strategy, we generate a two-dimensional capping layer on top of a standard three-dimensional Pb-Sn film. After capping, the surface defects can be passivated and the TACl-based two-dimensional perovskite effectively protected  $\text{Sn}^{2+}$  from oxidation, which stabilized the Sn-Pb perovskite composition, avoiding the Pb-based perovskite formation. It is further found that the TACl treatment suppressed the halide segregation and improved the perovskite film photostability. Cell efficiency increases from 16.25% to 18.28% and device life time ( $T_{80}$ ) increases from less than 100 hours to over 1000 hours. Our finding suggests that tuning ligand form/function represent a potentially highly productive direction to explore when trying to produce stable tin-based perovskite devices.

## TOC GRAPHICS



## Introduction

Considerable academic and industrial attention has recently been given to metal halide perovskites. To date solar cells, light emitting diodes, transistors, lasers, and detectors have all been demonstrated using the perovskite material system.<sup>1-5</sup> However, light harvesting remains one of the most promising applications due to the exceptionally high power conversion efficiencies (PCEs) coupled with the ability to deposit these materials using high-speed low cost printing processes.<sup>6-8</sup> One major drawback of current high efficiency perovskite solar cells is their high lead content which when coupled with their water solubility has the potential to cause a significant environmental hazard. Alternative nontoxic perovskites based on tin have shown promise but after years of development these materials still lag far behind the lead-based counterparts in terms of stability.<sup>9-11</sup> Solar cells using a mixed lead-tin (Pb-Sn)-based perovskite have shown very good efficiency values exceeding 21%.<sup>12</sup> Furthermore, the bandgap bowing effect first reported by Kanatzidis and coworkers<sup>13</sup> indicates that Sn incorporation pushes the optical bandgap towards the ideal region (1.2~1.4 eV) of the Shockley-Queisser limit<sup>14</sup> and thus theoretically the inclusion of Sn can allow higher theoretical PCEs to be reached. However, the biggest challenge is the strong chemical oxidation tendency of  $\text{Sn}^{2+}$  to form  $\text{Sn}^{4+}$ . This leads to severe p-doping thus higher dark saturation current.<sup>15</sup> Furthermore, easy oxidation of  $\text{Sn}^{2+}$  also makes Pb-Sn perovskites more susceptible to defect formation when exposed to the atmosphere, heat or irradiation stresses.<sup>16</sup>

To tackle these drawbacks, considerable effort has been devoted to mitigate  $\text{Sn}^{2+}$  oxidation thus enhance the structural integrity. Mixed dimensional perovskite concepts have been extended into the low-bandgap Pb-Sn perovskites in recent years, with the low-dimensional perovskite not only raising the formation energy of  $\text{Sn}^{4+}$  defects but also providing a very high chemical

stability. This results in a physical barrier preventing moisture and oxygen ingress.<sup>17-19</sup> Large-volume amine ligands such as butyl amine (BA),<sup>17</sup> phenylethyl amine (PEA),<sup>18</sup> 3-(aminomethyl) piperidinium (3AMP)<sup>19</sup> have been introduced to form mixed dimensional Pb-Sn perovskites, achieving PCEs of over 20% with enhanced stability.<sup>19</sup> However, one drawback of using low-dimensional perovskites is that device performance will be dependent upon the orientation of perovskite planes.<sup>20</sup> Developing a simple and effective method where the need for exact orientation control of the low-dimensional perovskite planes can be relaxed is highly desirable for increasing efficiency/stability simultaneously.

In addition to engineering the structural dimensionality of the material, another approach is to inhibit  $\text{Sn}^{2+}$  oxidation by the inclusion of antioxidants. These antioxidants function as reactants and can either directly reduce  $\text{Sn}^{4+}$  back to  $\text{Sn}^{2+}$ , typically like tin powder,<sup>21-23</sup> or act as sacrificial agents that compete with the  $\text{Sn}^{2+}$  oxidation process. Hydrazide vapor,<sup>24</sup> hydroxybenzene sulfonic acid,<sup>25</sup> gallic acid<sup>26</sup> have all been demonstrated to be effective in this regard because the reducing functional groups such as phenolic hydroxyl groups and hydrazide group can donate hydrogen atoms and electrons to scavenge oxygen. Combining the two concepts by creating 2D ligands equipped with reducing function groups would offer a two-pronged approach for solving the Pb-Sn based perovskite stability issue, however up to now there's few reports demonstrating this combination.

Here we propose that amine ligands based on phenol hydroxyl derivatives, which have previously been reported to suppress the  $\text{Sn}^{2+}$  oxidation,<sup>25-27</sup> can be designed to encourage the formation of a 2D perovskite phase and be incorporated into the 3D Pb-Sn perovskite structure. At the same time, the introduction of hydroxyl also brings other potential advantages such as

defect passivation,<sup>28</sup> enhanced electronic coupling of perovskite 2D sheets,<sup>29</sup> and suppressed ions migration,<sup>30</sup> thereby increasing device performance.

In this work, we employ the tyramine (TA) as bulky ligand to incorporate 2D perovskites in a 3D Pb-Sn perovskite structure for the first time. Our results indicate that low levels of tyramine-based 2D perovskite formed on the Pb-Sn perovskite surface can improve device efficiency and significantly prolong lifetime. We find the major advantages of tyramine application include; surface defects passivation; a protection against Sn<sup>2+</sup> oxidation; and suppression of halide segregation. Champion device efficiency increased from 16.25% to 18.28%, while the encapsulated 2D/3D device showed significantly improved T<sub>80</sub> life time from 100 h to over 1000 h after being stored in air. It is our hope that this work will open up a new pathway toward the fabrication of highly efficient and stable Pb-Sn binary solar cells using designed ligands that can prevent Sn<sup>2+</sup> oxidation.

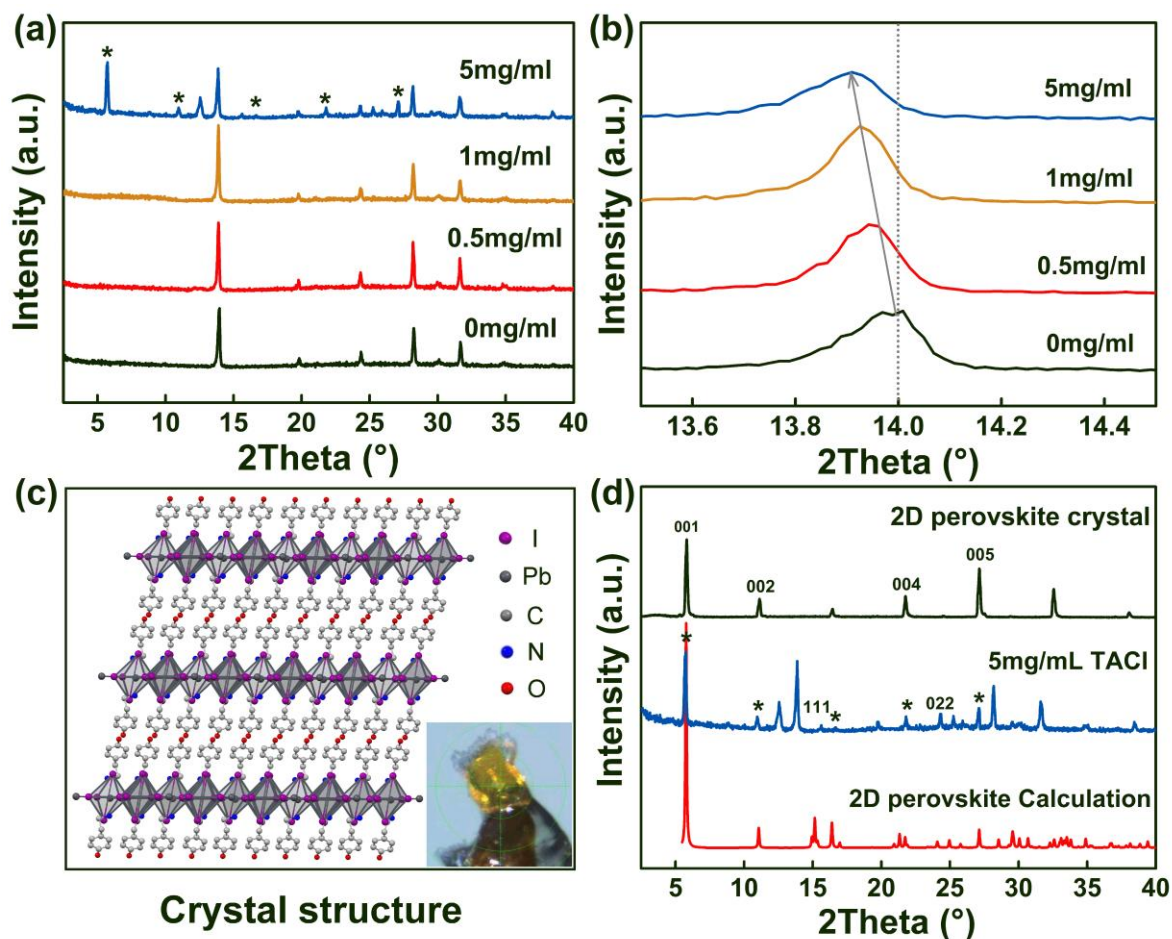
## **Results and discussion**

### **Tyramine-based 2D perovskite formation**

In this work, we use the FA<sub>0.85</sub>MA<sub>0.15</sub>Pb<sub>0.7</sub>Sn<sub>0.3</sub>I<sub>2.55</sub>Br<sub>0.45</sub> perovskite as the 3D light harvesting layer in our cell as it has a near-idea bandgap of ~ 1.34 eV (Figure S1). We obtained a pinhole-free  $\alpha$ -phase Pb-Sn binary perovskite layer by using chlorobenzene as an anti-solvent (SI for full details). After perovskite preparation, tyramine was introduced to the material by post-treating the Pb-Sn perovskite surface with TACl isopropanol solution in concentrations ranging from 0.1 mg mL<sup>-1</sup> to 5 mg mL<sup>-1</sup>. Figure 1a shows the X-ray diffraction (XRD) pattern of the resulting perovskite films. No obvious differences in the XRD pattern of TACl-treated perovskite films can be seen until the concentration is increased to 5 mg mL<sup>-1</sup>. This is consistent with the morphology evolution revealed by scanning electron microscopy (SEM) (Figure S2). The film

treated with 5 mg mL<sup>-1</sup> TACl solution shows a series of new peaks (marked with \*). These peaks, especially the peaks at small angles indicate the formation of a 2D layered perovskite phase.<sup>31,32</sup> The diffraction peak at around 12.6° indicates that the treatment leads to partial decomposition of the surface, promoting the 2D perovskite formation by a ligand exchange reaction between MA<sup>+</sup>/FA<sup>+</sup> cation and tyramine cation. Figure 1b shows an enlarged image of the peak near 14°, which corresponds to (110) lattice plane. It shows clear shift toward small angle (from 14.02° to 13.84°) as TACl concentration increases. This coincides with the increased lattice constant after including bulky tyramine cations. To provide further evidences demonstrating the 2D perovskite formation, we separately synthesized pure lead, tyramine-based 2D perovskite single crystals through cooling crystallization. We choose lead as source because of the higher proportion of Pb in the Pb-Sn perovskite. The resulting crystal structure is shown in Figure 1c while the XRD result of one of these highly pure crystals is shown in Figure 1d. It can be seen that the crystalline structure comprises of a typical 2D perovskite structure with the inorganic slabs is sandwiched by organic tyramine cation layer. Figure 1d depicts the simulated powder XRD patterns based on the refined crystal structure and the experimental XRD results of the layered crystal. Based on crystal data, we can assign the peaks observed in experimental XRD results to the typical (00k) lattice planes reflections. It indicates that the layered crystal grows parallel to the substrate which is consistent with what has been previously reported.<sup>33</sup> The peaks that emerge after TACl treatment coincide with that of the pure 2D layered perovskite crystal. This supports the notion that the application of TACl at 5 mg mL<sup>-1</sup> encourages the formation of the 2D perovskite phase. It is also worth noting that besides the dominant (00k) peaks, the perovskite film treated with TACl also show other peaks which correspond with (111), (022) lattice planes. This indicates that randomly orientated 2D perovskite domains also form on the 3D perovskite

surface.



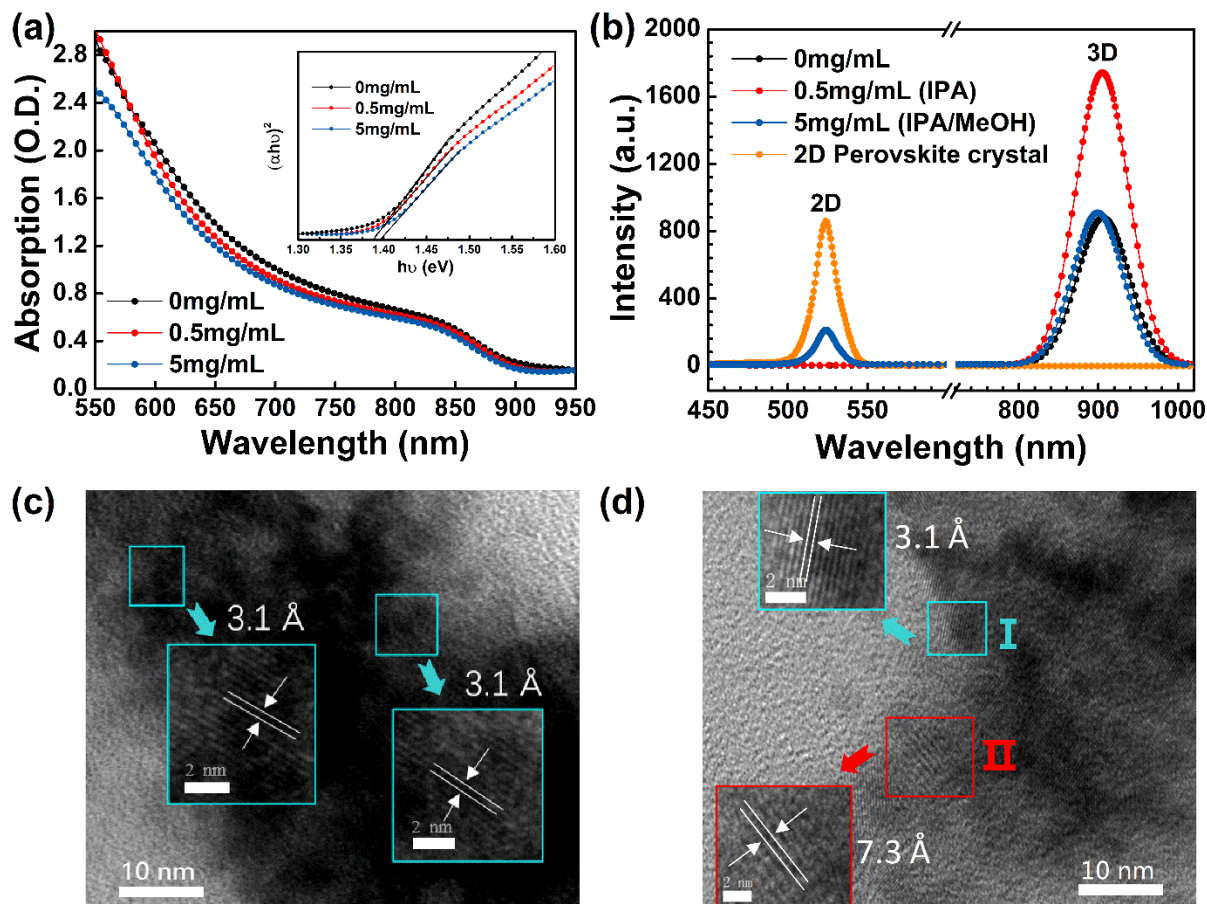
**Figure 1.** a) XRD pattern of Pb-Sn perovskite treated with different concentration TACl solution. b) An enlarged image of the peak near  $14^\circ$  of Figure 1a. c) crystal structure of TA-based 2D layered perovskite. d) XRD pattern of TACl based 2D perovskite crystal and the Pb-Sn perovskite film treated with  $5 \text{ mg mL}^{-1}$  TACl solution, the simulated powder XRD patterns based on the refined crystal structure is added for reference.

Figure 2a shows the UV-Vis absorption spectrum of Pb-Sn perovskite film treated with solutions containing  $0 \text{ mg mL}^{-1}$ ,  $0.5 \text{ mg mL}^{-1}$  and  $5 \text{ mg mL}^{-1}$  TACl solution. The derived Tauc plots, which enable the optical bandgap to be determined are shown inset within this figure. The

optical bandgap of  $\text{FA}_{0.85}\text{MA}_{0.15}\text{Pb}_{0.7}\text{Sn}_{0.3}\text{I}_{2.55}\text{Br}_{0.45}$  is around  $\sim 1.38$  eV which is near ideal according to Shockley and Queisser theory.<sup>14</sup> The absorption edge shows a slight blue shift as concentration is increased. Figure 2b plots the steady-state photoluminescence (PL) spectra of the TACl-treated perovskite films along with the PL response of the 2D crystal as a reference. A sharp PL peak can be seen at  $\sim 525$  nm, which is signature of excitonic emission from low-dimensional perovskites,<sup>34</sup> this is only observed in the 2D crystal and the film treated with  $5 \text{ mg mL}^{-1}$  TACl. This provides further evidence of 2D TACl-based perovskite formation. For the peak at around 900 nm which is ascribed to the emission from  $\text{FA}_{0.85}\text{MA}_{0.15}\text{Pb}_{0.7}\text{Sn}_{0.3}\text{I}_{2.55}\text{Br}_{0.45}$  three-dimensional perovskites.<sup>35</sup> Under low TACl concentrations ( $0.5 \text{ mg mL}^{-1}$ ) the peak at  $\sim 905$  nm is significantly enhanced. It is well known that for perovskite material, defects that create deep levels usually act as the predominant trap sources for non-radiative recombination losses.<sup>36,37</sup> Experimental results have further confirmed that deep-level defects exist in perovskite films,<sup>38,39</sup> and halide vacancies (such as  $V_{\text{I}}$ , under-coordinated Pb atoms) are the predominant contributors.<sup>40</sup> This enhanced 905 nm PL response upon  $0.5 \text{ mg mL}^{-1}$  TACl treatment suggests that the TACl passivates the surface deep-level defects due to the formation of 2D perovskite. When treating films with a high concentration ( $5 \text{ mg mL}^{-1}$ ) of TACl the PL display a blue-shift at 899 nm, which is consistent with the slightly larger bandgap observed in Figure 2a (inset). The PL intensity reduced compared with that in  $0.5 \text{ mg mL}^{-1}$  case. This is because we use isopropanol/methanol (solvent) to dissolve TACl. The polar methanol dissolving the organic halogen salt (Figure S3) leaves more halide vacancies, which may weaken the passivation effect of 2D perovskite.

From the above results we only obtained evidence that a 2D perovskite formed at high TACl concentrations, however the best-performing solar cells were obtained with  $0.5 \text{ mg mL}^{-1}$  TACl

treatment (Figure S4, Table S2). In order to give convincing evidence proving that the formation of 2D phase at 0.5 mg/mL TACl treatment, high-resolution transmission electron microscope (HRTEM) images of the control film and 0.5 mg/mL TACl treated films were measured and these results are shown in Figure 2c, d. Only one region (I, turquoise) with uniform lattice fringe and spacing features is observed in the control film. The interlayer spacing of 3.1 Å corresponds to the 3D perovskite phase.<sup>33</sup> While the TACl-treated film exhibited two regions (I and II) with different interlayer spacing. To further identify region II (red), we analyzed the interlayer distance of region II combining with the TACl-based 2D perovskite crystal data. The single crystal XRD pattern based on the refined crystal structure exhibited clear reflection peaks assigned to (00k) lattice plane of the n = 1 2D perovskite (Figure 1d). The diffraction peak at  $2\theta = 6.36^\circ$  was indexed to the (001) plane, which determines the unit cell dimension to be 13.76 Å according to the Bragg's equation  $d = n\lambda/2\sin\theta$ . By subtracting thickness of the inorganic octahedron (6.2 Å), the bulky cation spacing distance of n = 1 TACl-based 2D perovskite can be determined to be 7.56 Å, which is basically close to the interlayer spacing (7.3 Å) of region II. This indicates that a 2D phase indeed formed upon 0.5 mg/mL TACl treatment. But the amount of 2D perovskite is below the detection limit (XRD, PL etc.). One reason why the conventional 2D/3D concept has not been widely used is that it is difficult to suppress face-on packing within the 2D layer which has been associated with poor charge transport.<sup>20</sup> Thus by using an ultra-thin 2D perovskite capping layer we have demonstrated surface passivation while still maintaining efficient charge extraction.



**Figure 2.** a) UV-Vis absorption spectra of perovskite films treated with a range TACl solutions, the Tauc plots to determine optical band gap are inset. b) Steady-state PL spectra of perovskite films treated with different TACl solution, and TACl based 2D crystal. HRTEM image of the c) control Pb-Sn perovskite film and d) treated with  $0.5 \text{ mg mL}^{-1}$  TACl film.

### Suppressing $\text{Sn}^{2+}$ oxidation of Pb-Sn film

To investigate if the  $\text{Sn}^{2+}$  oxidation process can be slowed by the presence of tyramine, we prepared  $\text{Sn}^{2+}$  ( $\text{SnI}_2$ ) solutions without and with TACl and left them exposed to air for one day. The result can be seen in Figure 3a, the pure  $\text{Sn}^{2+}$  solution gradually turned from light yellow to brown after exposure to air, while the solution of TACl and  $\text{Sn}^{2+}$  remains light yellow. Figure S5 shows the NMR spectra of TACl and TACl- $\text{SnI}_2$  mixture in  $\text{D}_6$ -DMSO solvent. The obvious chemical shift of resonance signal belonging to hydrogen of  $\text{NH}_3^+$  from  $\delta=7.99 \text{ ppm}$  to  $\delta=7.71$

ppm was observed after blending TACl with SnI<sub>2</sub>. This indicates that the efficient coordination between TACl and SnI<sub>2</sub> and the possible formation of perovskite cluster in the solution. Such complexes has also been reported to prevent the Sn<sup>2+</sup> oxidation.<sup>41</sup> The oxidation which happens in the 3D Pb-Sn film upon exposure to air can be detected by measuring the Sn<sup>4+</sup> content using X-ray photoelectron spectroscopy (XPS). Figure 3b and Figure 3c plot the XPS Sn 3d<sub>3/2</sub> spectra of the control and TACl-treated perovskite film. This can be deconvolved into two individual peaks at 486.7 and 487.5 eV associated with Sn<sup>2+</sup> and Sn<sup>4+</sup> components. This allows us to calculate the surface Sn<sup>4+</sup> content and track the oxidation process in the pristine and TACl modified Pb-Sn films. We can see that the fresh films exhibit Sn<sup>4+</sup> an signal even though the film was made in a glovebox filled with N<sub>2</sub>. This ratio is 13.4% for the control Pb-Sn film and after TACl treatment the surface Sn<sup>4+</sup> component reduces to 7.9%. Suggesting that TACl can reduce Sn<sup>4+</sup> immediately upon treatment. Throughout the experiments, the TACl treated films experiment exhibited much weaker Sn<sup>4+</sup> signal compared to the control films when exposed to air, indicating higher resistance to Sn<sup>2+</sup> oxidation. Figure 3d summarizes the Sn<sup>4+</sup> percentage as a function of storage time. At 10 days, the Sn<sup>4+</sup> fraction of the control sample was almost 70%, while in the treated sample this figure was only at 24.1%. This demonstrates that the TA based 2D perovskite capping layer suppressed the Pb-Sn oxidation.

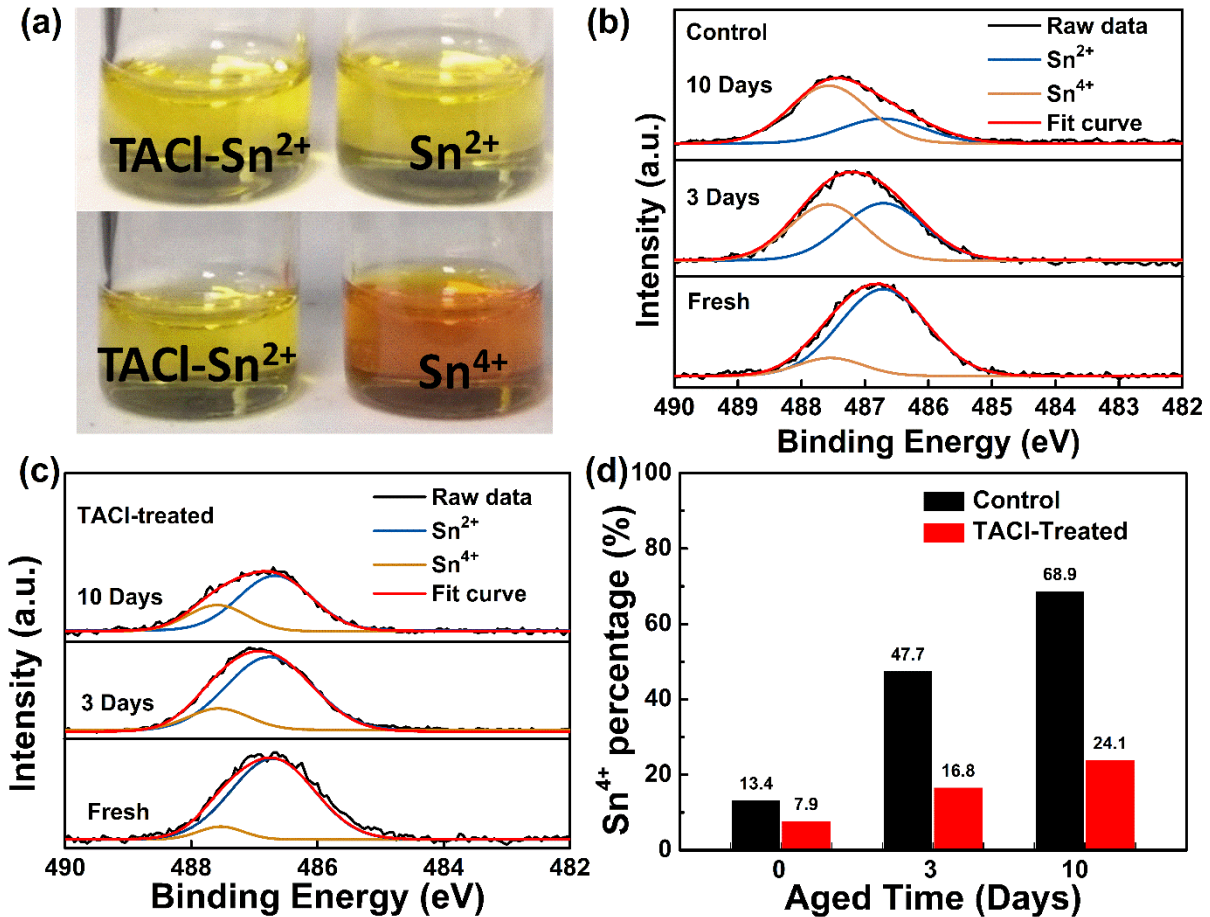


**Figure 3** a) Pictures of SnI<sub>2</sub> and SnI<sub>2</sub>-TACl solution stored in air (open, room temperature, 25% relative humidity for one day). b) XPS Sn 3d spectra of the control and (c) TACl-treated Pb-Sn perovskite films stored in air for 0 days, 3 days and 10 days (25% relative humidity, room temperature). The Sn 3d<sub>3/2</sub> peak is deconvoluted into two individual peaks at 486.7 (blue lines) and 487.5 eV (orange lines) associated with Sn<sup>2+</sup> and Sn<sup>4+</sup> components. d) The atomic ratio of Sn<sup>4+</sup> derived from the XPS Sn 3d spectra.

### Passivation of the 3D film from tyramine-based 2D perovskite

In order to further understand how the TACl treatment affects the electronic properties of the film, we investigate the charge-carrier dynamics using steady-state PL and time-resolved photoluminescence (TRPL) spectroscopy. Figure 4a depicts the PL and absorption spectra of Pb-

Sn perovskite films without and with 0.5 mg mL<sup>-1</sup> TACl treatment. Pb-Sn based binary perovskite films exhibit a PL peak at 905 nm, corresponding to the absorption band edge. TACl treatment doesn't change the position of the emission peak but does increase its intensity by a factor of two. The absorption intensity remains almost the same before and after treatment, indicating the optical characteristics of the material don't change. Therefore, this significantly enhanced PL response suggests that TACl treatment passivates surface trap states thus reduces the non-radiative recombination, as mentioned above. Two typical TRPL transients of the treated and untreated films are presented in Figure 4b. According to the bi-exp. fitting,<sup>42</sup> an average carrier lifetime of 418.4 ns and 545.6 ns can be extracted for the control film and the TACl treated film respectively, an overview of the curves can be found in Table S1. The longer carrier lifetime suggests a less radiative recombination and therefore fewer trap states and hence a better electronic film quality.

To quantitatively understand how the electronic trap density changes upon TACl treatment, we conduct space charge limited current (SCLC) measurements and thermal admittance spectroscopy (TAS).<sup>39,43</sup> Figure 4c shows the dark I-V curves of hole-only devices with and without TACl treatment. The plot clearly shows the three classic SCLC transport regions, Ohmic, Trap-filled and space charge limited as indicated on the top of the graph. As the curves transition from the Ohmic to the trap-filled region ( $V_{TFL}$ ), we can observe a steep rise in current. Using the equation  $2\varepsilon_r\varepsilon_0V_{TFL} = eN_{trap}L^2$  to estimate the trap density, we obtain a value of  $4.5 \times 10^{15} \text{ cm}^{-3}$  for the control device and a value of  $2.2 \times 10^{15} \text{ cm}^{-3}$  for the TACl treated device. We estimated the hole mobility by fitting dark I-V curves to the Mott-Gurney relation.<sup>44</sup> The calculated hole mobilities of perovskite film increased from  $8.21 \times 10^{-4} \text{ cm}^2/\text{Vs}$  (control) to  $3.94 \times 10^{-3} \text{ cm}^2/\text{Vs}$  upon TACl treatment (Figure S6). This is consistent with the increased carrier mobility predicted

by gpvdm modeling discussed below. Figure 4d shows the thermal admittance spectroscopy spectra for samples with and without TACl treatment. From this figure, one can see that the TACl-treated film has a lower trap density by one order of magnitude between 0.33 and 0.39 eV. Previously results such as these have been attributed to the passivation of deep-level defects.<sup>45</sup> Thus, we conclude that TACl effectively diminish surface deep-level defects due to the formation of 2D perovskite.

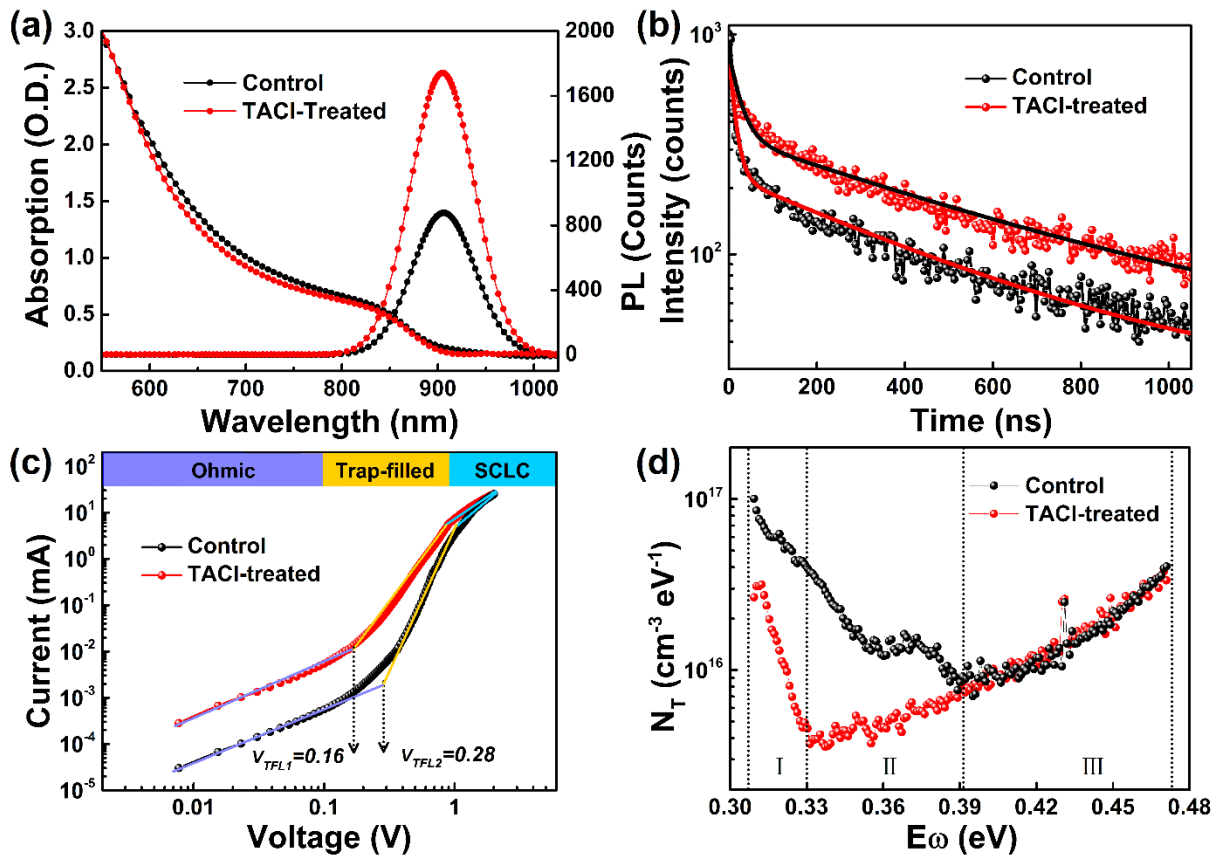


**Figure 4.** a) Steady-state absorption and PL spectra of pristine and TACl-treated Pb-Sn perovskite film on quartz, in the PL measurement the samples were excited from film side using 405 nm laser. b) time-resolved PL spectra of pristine and TACl-treated Pb-Sn perovskite film on quartz, 405 nm 100ps laser pulse was used for the excitation source. c) Dark I-V curves of hole-

only device based on pristine and TACl-treated Pb-Sn perovskite film. d) The trap density obtained by TAS for devices based on pristine and TACl-treated Pb-Sn perovskite film.

### **Inhibited phase segregation in Pb-Sn film**

Figure 5a depicts PL spectra taken from a control and TACl treated perovskite films. After 40 min exposure to air the PL peak at  $\sim 900$  nm of control film is reduced and a pronounced emission peak at 770 nm appears. This 770 nm emission is characteristic of the pure Pb-based perovskite phase.<sup>46</sup> To further clarify the reason for the newly-emerged peak, we measured the PL spectra of control film at 0 min and 40 min stored under N<sub>2</sub> conditions, as shown in Figure S7. No peak at 770 nm was detected, and the main PL peak was also basically unchanged upon N<sub>2</sub> exposure. This demonstrates that the PL changes may originate from the composition variation caused by Sn<sup>2+</sup> oxidation. By contrast, upon aging there is no obvious change in the 2D/3D perovskite film treated with TACl. This indicates that The TACl-based 2D perovskite would appear to serve as a protecting layer thereby helping to stabilize the Sn-Pb binary composition. XRD characterization was performed to verify this hypothesis. Figure 5b plots the diffraction peak at 14° of a control Pb-Sn perovskite film, the peaks shift toward lower 2 $\theta$  angles over the measurement time. This is consistent with the larger sized Pb<sup>2+</sup> cation occupying the B-sites in the perovskite lattice. Whereas the TACl treated 2D/3D film remain stable.

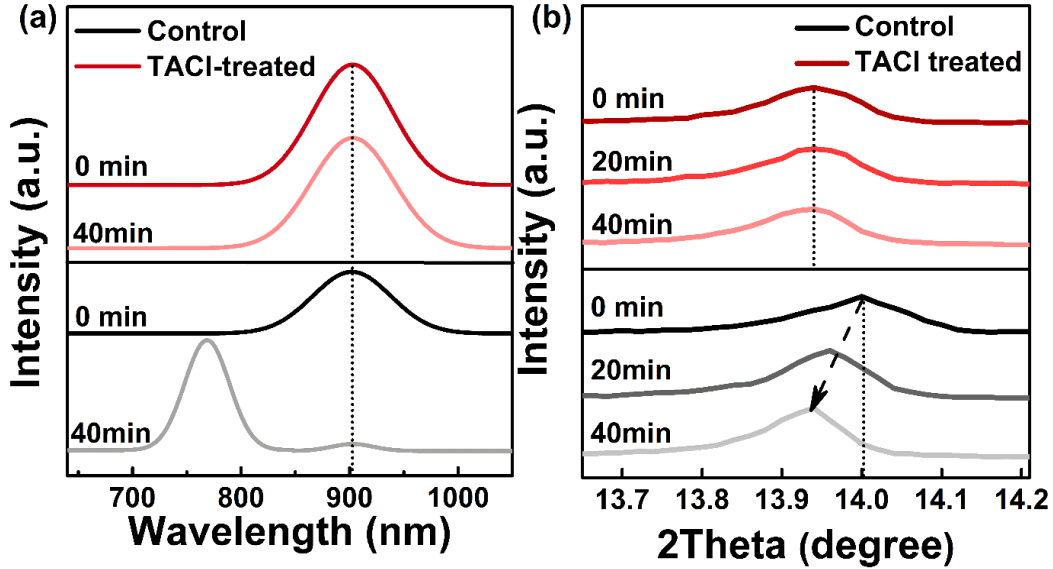


**Figure 5.** a) The steady-state PL spectra of control and TACl-treated Pb-Sn perovskite film in their very beginning and exposure for 40 min, emission peak at 770 nm corresponds to pure Pb-based perovskite phase, may be  $\text{MAPbI}_3$  or  $\text{MA}_x\text{FA}_{(1-x)}\text{PbI}_y\text{Br}_{(3-y)}$ , emission peak at 900 nm corresponds to Pb-Sn binary perovskite. b)  $14^\circ$  XRD peak evolution over the measurement time of control and TACl-treated Pb-Sn perovskite film.

The light-induced halide segregation in mixed-halide perovskite is also one critical issue that limits the stability of PSCs. In order to evaluate the effect of TACl treatment on halide segregation, we carried out illumination durable test under  $\text{N}_2$  conditions by monitoring the PL and XRD spectra of control and TACl-treated perovskite films. Figure 6 shows the recorded PL and XRD curves of perovskite films at different illumination time. For control Sn-Pb film, the PL peak of perovskite showed a slight red shift from 904 nm (0 min) to 907 nm (10 min) and then almost fixed at  $\sim 909$  nm when extended the illumination time to 40 min, which indicates the formation of lower bandgap I rich domains. In contrast, the TACl treated film shows a smaller shift only from 904 nm to 905 nm, demonstrating the suppressed halide segregation and improved photostability. XRD test showed similar results. The (110) and (220) diffraction peaks

of control film showed a shift to lower  $2\theta$  angles ( $14.00^\circ$  to  $13.95^\circ$ ) over the illumination time while the TACl-treated sample showed negligible shift, demonstrating the improved film photostability.

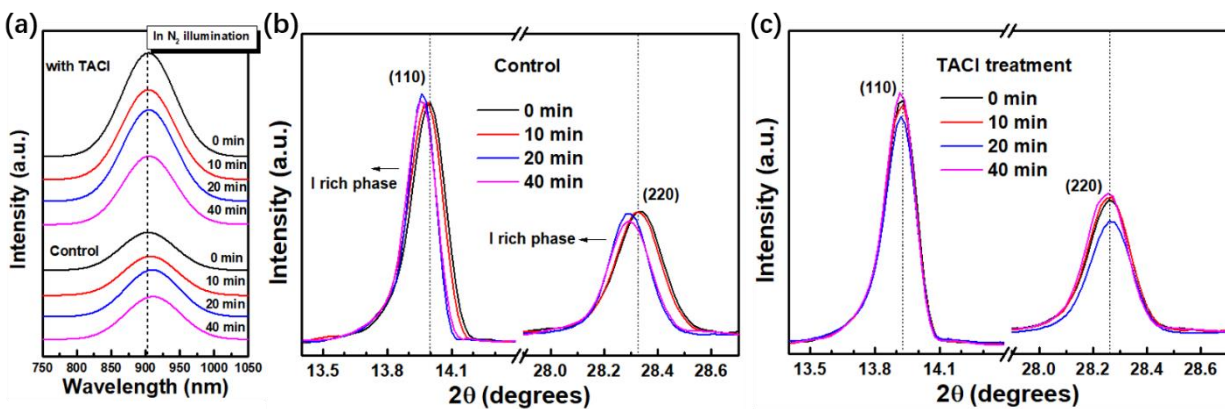


**Figure 6.** a) PL spectra of control film and TACl-treated film under  $N_2$  condition with different illumination time. (110) and (220) diffraction peak of control film (b) and TACl-treated film (c) under  $N_2$  condition with different illumination time. The samples were irradiated with 439 nm laser source for different time. The excitation level is estimated to be around  $5 \text{ mW/cm}^2$ .

### Photovoltaic performance

To understand how these perovskite films perform in photovoltaic devices inverted planar heterojunction solar cells were fabricated using treated and untreated  $\text{FA}_{0.85}\text{MA}_{0.15}\text{Pb}_{0.7}\text{Sn}_{0.3}\text{I}_{2.55}\text{Br}_{0.45}$  (Figure S4, Table S2). Figure 7a shows the current density-voltage ( $J$ - $V$ ) curves of the best-performing control and TACl-treated perovskite solar cells in reverse and forward bias mode (the dots are experimental data, the lines are simulation which will be discussed later), detailed photovoltaic parameters are listed in Table S3. The control device shows better performance under forward scan, with a PCE of 16.25%, open-circuit voltage ( $V_{oc}$ ) of 0.82 V, short-circuit current density ( $J_{sc}$ ) of  $27.10 \text{ mA cm}^{-2}$ , and fill factor ( $FF$ ) of 0.73. (See SI for further tabulated results). When the solar cells are treated with optimal TACl of

0.5 mg mL<sup>-1</sup> the  $J$ - $V$  curves shows negligible hysteresis (forward PCE of 18.28%, reverse PCE of 18.10%) and an improved PCE of 18.28% with a  $V_{oc}$  of 0.85 V, a  $J_{sc}$  of 27.36 mA cm<sup>-2</sup>, and an  $FF$  of 0.79. Figure 7b shows the steady-state photocurrent and power output of best TACl-treated device. A stabilized output of 18.11% over 2200 s was observed, which is very close to the PCE value recorded from the  $J$ - $V$  curves. Figure 7c shows the histogram of efficiency based on 20 devices, devices produced under the same conditions are clumped together and have efficiencies of within a few percent of each other demonstrating the repeatability of our fabrication and measurements. In Figure 7d we compare the shelf stability of encapsulated Pb-Sn perovskite solar cells without and with TACl treatment. The devices were stored in dark in air with a relative humidity of 25±5%. We observed that the TACl-treated devices exhibited superior shelf stability and retained 85% of their efficiency after 1000 h while the control device exhibited a quick decrease of efficiency within 400 h. We attribute the improved stability to the protecting TACl based 2D perovskite suppressing Sn<sup>2+</sup> oxidation.

We also carried out contrast experiments in which the TACl was introduced into perovskite precursor solution. The TACl doping amount was controlled within 1% (molar ratio relative to 3D perovskite) to make sure it is trace amount introduction and avoid the 2D phase formation in the final perovskite film.<sup>47</sup> Through this comparison we may be able to better understand the role of TACl-based 2D phase in enhancing device behavior. Figure S8 and Table S4 shows the photovoltaic performance results. We observed noticeable performance improvement when adding 0.1% TACl into the precursor with the PCE increased from 15.93% to 17.42%. This value further increased to 17.87% when adding 0.3% TACl, which is basically comparable with the best PCE obtained in post-treatment scenario. We attributed the enhanced  $V_{oc}$  and fill factor to that the TACl effectively passivates defects at perovskite grain boundaries through

coordination effect. We further measured the shelf stability of encapsulated Pb-Sn perovskite solar cells without and with 0.3% TACl. It is found that TACl doping also improved the device stability, but the efficacy is significantly weaker than the post-treatment. After around 300 h the post-treated devices still maintained 88% of their initial efficiency while precursor doping devices remained 71%. From this it can be seen that the formation of TACl-based 2D perovskite phase plays a dominant role in improving the device performance especially boosting the device stability. This ultrathin 2D perovskites may act as capping layer thus suppress the water/oxygen ingress from the surface, which provides additional protection for the  $\text{Sn}^{2+}$  oxidation.

The charge recombination dynamics of both devices were probed by using a combination of electrical and optical measurements. Figure 7e right shows the Suns- $J_{sc}$  curves. By fitting equation  $J_{sc} \propto I^\alpha$  it was found that both devices had an  $\alpha$  value close to unity, which signifies that the devices have efficient carrier sweep-out.<sup>48</sup> Figure 7e left plots the  $V_{oc}$  versus light intensity. The Suns- $V_{oc}$  curve had a higher linear slope ( $1.73kT q^{-1}$ ) for the control device than that ( $1.56kT q^{-1}$ ) of TACl-treated device, indicating more electronic disorder and trap-assisted recombination losses in the system.<sup>49</sup> This is consistent with it being more susceptible to defect (Sn vacancies) formation as a result of  $\text{Sn}^{2+}$  oxidation as outlined above. Transient photovoltage measurements (TPV) were performed under background lighting, guaranteeing the baseline basically equals to  $V_{oc}$  of the solar cells. The results can be seen in Figure 7f. The TPV transients for the TACl-treated device exhibited a single exponential decay with lifetime of 3.6  $\mu\text{s}$  compared to 2.1  $\mu\text{s}$  for the untreated device. The extended recombination could explain the enhanced  $V_{oc}$ .

Lastly, to better understand the electrical measurements in terms of material parameters, the general-purpose photovoltaic device model (gpvdm), a non-equilibrium Shockley-Read-Hall

(SRH) based drift diffusion model<sup>50-52</sup> was fit to the experimental data. The model solves, the bipolar drift diffusion, Poisson's, the SRH capture escape/recombination equations and as well as solving the optical problem with the transfer matrix method. The model was fit self consistently to the light  $J-V$  (see Figure 7a), Suns- $J_{sc}$ , Suns- $V_{oc}$  (see Figure 7e), and TPV transients (see Figure 7f) using a single set of material parameters for each device. Optical parameters for the model were taken from ellipsometry measurements, as shown in Figure S9. The extracted material parameters are shown in Table S5. It was found that for devices treated with TACl free carrier mobility increased by a factor of two, trap density decreased by a factor of two and carrier cross-sections without adversely affecting the interface properties (the series resistance, contact charge density), this is in line with our previous findings.

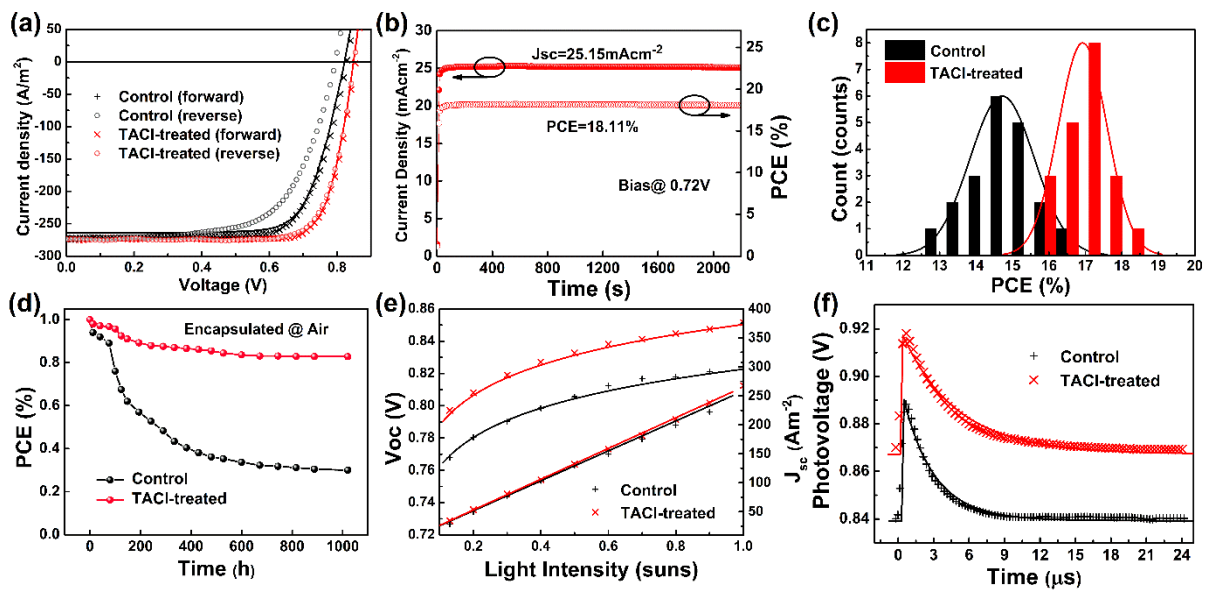


**Figure 7.** a)  $J-V$  curves of the optimal Pb-Sn perovskite solar cells without and with TACl treatment in reverse and forward scan. The plots are experimental data, the lines are simulation. b) Steady-state photocurrent and power output of best TACl-treated device, measured under AM1.5G illumination at 0.72 V. c) A histogram of the efficiency measured from 20 individual devices based on pristine and TACl-treated perovskite film. d) Shelf stability of encapsulated

control and TACl-treated devices stored in air with  $25\pm 5\%$  relative humidity. e)  $V_{oc}$  as a function of Light intensity. f) TPV transient of control and TACl-treated devices.

## **Conclusion**

In summary, we demonstrated that by carefully selecting the correct ligand treatment, stability and performance of Pb-Sn perovskite solar cells can be enhanced. By applying tyramine hydrochloride (TACl) to the surface of a 3D Pb-Sn film, an ultra-thin sheet of 2D perovskite was formed. We demonstrated the 2D perovskite layer plays three key roles; i) it provides effective surface defect passivation; ii) it stabilizes the lattice inhibiting  $\text{Sn}^{2+}$  oxidation; and iii) the typical halide segregation which often occurs in mix-halide perovskites is significantly suppressed. Solar cells made of the Pb-Sn binary material showed a champion PCE of 18.28% and only a 15% efficiency loss after 1000 hours in air. This work opens up new avenue through which to stabilize and explore the more environmentally friendly Pb-Sn material system.

## **Experimental Section**

### ***Materials***

All materials were used as received without further purification. PTAA was purchased from Xi'an Polymer Light Technology. The halide salts (FAI, MABr,  $\text{PbI}_2$ ,  $\text{PbBr}_2$ , with purity of  $>99.5\%$ ) were purchased Xi'an Polymer Light Technology.  $\text{SnI}_2$  (99.999%, lot no. 14476) were purchased from Alfa Aesar.  $\text{SnF}_2$  (99%, lot no. 334626), tyramine hydrochloride (99%) was purchased from J&K. DMF (99.8% anhydrous, lot no. 227056), DMSO (99.9% anhydrous, lot no. 276855), isopropanol (anhydrous, 99.5%) were purchased from J&K. Chlorobenzene (99.8% anhydrous, lot no. 284513) were purchased from Sigma-Aldrich. Hydriodic acid (57% w/w aq. soln., stab with 1.5% hypophosphorous acid) were purchased from Alfa Aesar. The  $\text{C}_{60}$ , BCP ( $>99\%$  sublimed) was purchased from Lumetic.

### ***Perovskite precursor solution***

For the narrow-bandgap FA<sub>0.85</sub>MA<sub>0.15</sub>Pb<sub>0.7</sub>Sn<sub>0.3</sub>I<sub>2.55</sub>Br<sub>0.45</sub> perovskite, the precursor solution (1.33 M) was prepared in mixed solvents of DMF and DMSO with a volume ratio of 4:1. 1.08 mmol FAI, 0.2 mmol MABr, 0.73 mmol PbI<sub>2</sub>, 0.4 mmol SnI<sub>2</sub>, and 0.2 mmol PbBr<sub>2</sub> were added into 1 mL DMF:DMSO mixed solvent. SnF<sub>2</sub> (10 mol% relative to SnI<sub>2</sub>) was added in the precursor solution. The precursor solution was stirred at room temperature for 2 h. Tin powders (5 mg mL<sup>-1</sup>) were added in the precursor to reduce Sn<sup>4+</sup> in the precursor solution. The precursor solution with the remaining tin powders was filtered through a 0.22 μm polytetrafluoroethylene (PTFE) membrane before making the perovskite films.

### ***Tyramine based 2D perovskite single crystal synthesis***

122.5 mg tyramine hydrochloride and 162.5 mg PbI<sub>2</sub> and 2 mL Hydriodic acid (aq. soln.) were added into a 10 mL Vial. This solution was heated and stirred at 75 °C to be fully dissolved. This solution is filtered through a 0.22 μm polytetrafluoroethylene (PTFE) membrane to obtain the mother liquor. The cooling crystallization procedure follows a cooling rate of 1 °C per 20 min and orange crystals appeared at 54 °C. The reactor was maintained at 54 °C for another 5 hours to allow the crystals to grow.

### ***Device fabrication and characterization***

The basic device structure is ITO/PTAA/ FA<sub>0.85</sub>MA<sub>0.15</sub>Pb<sub>0.7</sub>Sn<sub>0.3</sub>I<sub>2.55</sub>Br<sub>0.45</sub> (with or without TACl treatment)/C<sub>60</sub>/BCP/Ag. The patterned ITO glass substrates (15 ohm/square) were pre-cleaned by ultrasonic baths in detergent, deionized water, acetone, and isopropyl alcohol sequentially and transferred into a nitrogen-filled glove box (H<sub>2</sub>O and O<sub>2</sub> values < 0.5 ppm) for subsequent film deposition. 2mg mL<sup>-1</sup> PTAA was spun onto the ITO substrate at 6000rpm for 30s and annealed on 100 °C hot plate for 10min. Afterward, the perovskite precursor was spun at

1000 rpm for 10 s and 6000 rpm for 30 s. During the second stage, 100  $\mu\text{L}$  chlorobenzene with 6%  $\text{v}\text{v}^{-1}$  ACN was dropped on the center of the substrate at 16 s, and the obtained films were annealed at 120  $^{\circ}\text{C}$  for 60 min. A pinhole-free  $\alpha$ -phase Pb-Sn binary perovskite layer was obtained, as indicated in the following Figure S2a and Figure S3. The perovskite film thickness is around 480 nm, which is measured by the cross-sectional SEM image of the entire devices in Figure S10. The TACl with various concentrations was spun at 3000rpm onto the perovskite film for 30s and annealed at 100  $^{\circ}\text{C}$  10min. The devices were finally completed by thermal evaporation of a 20 nm thick  $\text{C}_{60}$  and 8 nm BCP and 90 nm thick silver (Ag) anode in vacuum (vacuum degree  $\approx 5\times 10^{-4}$  Pa). Hole-only devices were fabricated using configuration of ITO/PTAA/Pb-Sn perovskite/ $\text{MoO}_3$ /Au.

The current density-voltage ( $J$ - $V$ ) characteristics of fabricated devices were measured with a metal mask aperture to define the device active area to be about 0.064  $\text{cm}^2$  using Keithley 2601 Source Meter in the dark and under Air Mass 1.5 Global (AM 1.5 G) solar illuminations with an Oriel 300 W solar simulator intensity of 100  $\text{mW cm}^{-2}$  (denoted as 1 sun). The light intensity was measured by a photometer (International light, IL1400) and corrected by a standard silicon solar cell. The EQE spectra were conducted using Q-Test Station 1000 AD (Crowntech Inc. USA) with a standard silicon photovoltaic cell traced to the American National Standards Institute. The surface morphologies were characterized with scanning electron microscope (SEM, Horiba Scanning Electron Microscope.). The high-resolution transmission electron microscopy (TEM) was carried out using a Hitachi H-800 electron microscope at an acceleration voltage of 200 kV with a CCD camera. The X-ray diffraction (XRD) spectra were conducted on a Rigaku D/max-2500 X-ray diffraction meter with Cu  $\text{K}\alpha$  radiation ( $\lambda=1.5418\text{\AA}$ ). The UV-vis absorption spectra were carried out by using Shimadzu 3600 UV-visible-NIR spectrophotometer.

Photoluminescence (PL) and TRPL spectra was obtained using FLS980 with a picosecond diode laser excitation at a wavelength of 405 nm. in the PL measurement the samples were prepared on quartz and excited from film side. The laser pulse used for TRPL measurement is 405 nm 100ps. X-ray photoemission spectroscopy (XPS) experiments were carried out using a VG Scienta R3000 spectrometer in an ultrahigh vacuum at a base pressure of  $2 \times 10^{-10}$  mbar. The measurement chamber was equipped with monochromatized He (Ia) radiation at 21.2 eV and a monochromatic Al (K $\alpha$ ) X-ray source providing photons with 1486.6 eV. <sup>1</sup>HNMR spectra were recorded on an AVANCE 500 spectrometer with tetramethylsilane (TMS) as the standard. Impedance spectroscopy was measured by an Electrochemical Analyzer Meter (CHI 660E). The measurement condition for thermal admittance spectroscopy (TAS) is under 1 sun illumination, with 50mV of AC sinusoidal voltage and frequency ranging from 1 MHz to 1 Hz at short-circuit condition. The energetic profile of trap density of states (tDOS) can be derived from the angular frequency dependent capacitance using the equation:<sup>39</sup>

$$N_T(E_\omega) = - \frac{\omega V_{bi} dC}{Wqk_B T d\omega} \quad (1)$$

in which  $\omega$  is the angular frequency,  $V_{bi}$  and  $W$  are the built-in potential and the depletion width obtained from the Mott-Schottky curve,  $q$  is the elementary charge,  $k_B$  is Boltzmann's constant,  $C$  is the capacitance. The applied angular frequency  $\omega$  defines an energetic demarcation.<sup>39</sup>

$$E_\omega = -KBT \ln \frac{\omega_0}{\omega} \quad (2)$$

where  $\omega_0$  is the is the threshold angular frequency. For  $\omega < \omega_0$  the occupation of the defect can follow the applied AC signal and the charging and discharging of the defect contribute to the capacitance, whereas for high modulation frequencies the defects cannot follow and no contribution to the capacitance arises.  $\omega_0$  can be considered as a limit for which a defect can be

charged and discharged by the AC modulation. Unless otherwise specified, the characterizations were performed at 25±5% relative humidity and room temperature.

For the SCLC measurement, the hole only devices were fabricated with a device structure of ITO/PTAA/Pb-Sn perovskite/MoO<sub>3</sub>/Au. The dark I-V characteristic was plotted into a semi-log scale and fitted to a space charge limited form according to the formula<sup>44</sup>

$$J(V) = \frac{9}{8} \varepsilon \varepsilon_0 \mu \exp \left( 0.89 \beta \sqrt{\frac{V-V_{bi}}{L}} \right) \frac{(V-V_{bi})^2}{L^3} \quad (3)$$

in which J is the current density,  $\varepsilon_0$  is the permittivity of free space,  $\varepsilon$  is the relative permittivity of the material,  $\mu$  is the hole mobility, L is the thickness of the active layer, and  $V_{bi}$  is the built-in voltage.

#### ASSOCIATED CONTENT

**Supporting Information.** Gpvd simulation; EQE spectra; SEM images; EDS mapping; TACI concentration optimization; <sup>1</sup>HNMR spectra; Optical parameters

#### AUTHOR INFORMATION

Corresponding Author

\*E-mail: [sp\\_wen@jlu.edu.cn](mailto:sp_wen@jlu.edu.cn)

ORCID:

Shanpeng Wen: 0000-0001-5114-6307

#### Author Contributions

G. Wang<sup>#</sup> and C. Wang<sup>#</sup> contributed equally to this work as co-first authors.

The manuscript was written through contributions of all authors. All authors have given approval to the final version of the manuscript.

## Notes

The authors declare no competing financial interest.

## ACKNOWLEDGMENT

This work was supported by the National Natural Science Foundation of China (Grant No. 52073115), the Project of Science and Technology Development Plan of Jilin Province (Grant No. 20200201085JC), China Postdoctoral Science Foundation (Grant No. 2019M661208).

## REFERENCES

- (1) Jeong, J.; Kim, M.; Seo, J.; Lu, H.; Ahlawat, P.; Mishra, A.; Yang, Y.; Hope, M. A.; Eickemeyer, F. T.; Kim, M., Pseudo-Halide Anion Engineering for  $\alpha$ -FAPbI<sub>3</sub> Perovskite Solar Cells. *Nature* **2021**, *592*, 381-385.
- (2) Xu, W.; Hu, Q.; Bai, S.; Bao, C.; Miao, Y.; Yuan, Z.; Borzda, T.; Barker, A. J.; Tyukalova, E.; Hu, Z., Rational Molecular Passivation for High-Performance Perovskite Light-Emitting Diodes. *Nature Photonics* **2019**, *13*, 418-424.
- (3) Gedda, M.; Yengel, E.; Faber, H.; Paulus, F.; Kreß, J. A.; Tang, M. C.; Zhang, S.; Hacker, C. A.; Kumar, P.; Naphade, D. R., Ruddlesden-Popper-Phase Hybrid Halide Perovskite/Small-Molecule Organic Blend Memory Transistors. *Adv. Mater.* **2021**, *33*, 2003137.

- (4) Qin, C.; Sandanayaka, A. S.; Zhao, C.; Matsushima, T.; Zhang, D.; Fujihara, T.; Adachi, C., Stable Room-Temperature Continuous-Wave Lasing in Quasi-2D Perovskite Films. *Nature* 2020, *585*, 53-57.
- (5) Wei, H.; Fang, Y.; Mulligan, P.; Chirazzini, W.; Fang, H.-H.; Wang, C.; Ecker, B. R.; Gao, Y.; Loi, M. A.; Cao, L., Sensitive X-ray Detectors Made of Methylammonium Lead Tribromide Perovskite Single Crystals. *Nature Photonics* 2016, *10*, 333-339.
- (6) Qin, M.; Xue, H.; Zhang, H.; Hu, H.; Liu, K.; Li, Y.; Qin, Z.; Ma, J.; Zhu, H.; Yan, K., Precise Control of Perovskite Crystallization Kinetics via Sequential A-site Doping. *Adv. Mater.* 2020, *32*, 2004630.
- (7) Hui, W.; Chao, L.; Lu, H.; Xia, F.; Wei, Q.; Su, Z.; Niu, T.; Tao, L.; Du, B.; Li, D., Stabilizing Black-Phase Formamidinium Perovskite Formation at Room Temperature and High Humidity. *Science* 2021, *371*, 1359-1364.
- (8) Li, N.; Niu, X.; Li, L.; Wang, H.; Huang, Z.; Zhang, Y.; Chen, Y.; Zhang, X.; Zhu, C.; Zai, H., Liquid Medium Annealing for Fabricating Durable Perovskite Solar Cells with Improved Reproducibility. *Science* 2021, *373*, 561-567.
- (9) Shao, S.; Liu, J.; Portale, G.; Fang, H. H.; Blake, G. R.; ten Brink, G. H.; Koster, L. J. A.; Loi, M. A., Highly Reproducible Sn-Based Hybrid Perovskite Solar Cells with 9% Efficiency. *Adv. Energy Mater.* 2018, *8*, 1702019.
- (10) Liu, X.; Wu, T.; Chen, J.-Y.; Meng, X.; He, X.; Noda, T.; Chen, H.; Yang, X.; Segawa, H.; Wang, Y., Templated Growth of FASnI<sub>3</sub> Crystals for Efficient Tin Perovskite Solar Cells. *Energy & Environ. Sci.* 2020, *13*, 2896-2902.

- (11) Jiang, X.; Wang, F.; Wei, Q.; Li, H.; Shang, Y.; Zhou, W.; Wang, C.; Cheng, P.; Chen, Q.; Chen, L., Ultra-high Open-Circuit Voltage of Tin Perovskite Solar Cells via An Electron Transporting Layer Design. *Nature Commun.* 2020, *11*, 1-7.
- (12) Kapil, G.; Bessho, T.; Maekawa, T.; Baranwal, A. K.; Zhang, Y.; Kamarudin, M. A.; Hirotsu, D.; Shen, Q.; Segawa, H.; Hayase, S., Tin-Lead Perovskite Fabricated via Ethylenediamine Interlayer Guides to the Solar Cell Efficiency of 21.74%. *Adv. Energy Mater.* 2021, 2101069.
- (13) Hao, F.; Stoumpos, C. C.; Chang, R. P.; Kanatzidis, M. G., Anomalous Band Gap Behavior in Mixed Sn and Pb Perovskites Enables Broadening of Absorption Spectrum in Solar Cells. *J. Am. Chem. Soc.* 2014, *136*, 8094-8099.
- (14) Shockley, W.; Queisser, H. J., Detailed Balance Limit of Efficiency of p-n Junction Solar Cells. *J. Appl. Phys.* 1961, *32*, 510-519.
- (15) Li, C.; Song, Z.; Zhao, D.; Xiao, C.; Subedi, B.; Shrestha, N.; Junda, M. M.; Wang, C.; Jiang, C. S.; Al-Jassim, M., Reducing Saturation-Current Density to Realize High - Efficiency Low-Bandgap Mixed Tin-Lead Halide Perovskite Solar Cells. *Adv. Energy Mater.* 2019, *9*, 1803135.
- (16) Gu, S.; Lin, R.; Han, Q.; Gao, Y.; Tan, H.; Zhu, J., Tin and Mixed Lead-Tin Halide Perovskite Solar Cells: Progress and Their Application in Tandem Solar Cells. *Adv. Mater.* 2020, *32*, 1907392.

- (17) Ramirez, D.; Schutt, K.; Wang, Z.; Pearson, A. J.; Ruggeri, E.; Snaith, H. J.; Stranks, S. D.; Jaramillo, F., Layered Mixed Tin-Lead Hybrid Perovskite Solar Cells with High Stability. *ACS Energy Lett.* 2018, 3, 2246-2251.
- (18) Ruggeri, E.; Anaya, M.; Gałkowski, K.; Delpont, G.; Kosasih, F. U.; Abfalterer, A.; Mackowski, S.; Ducati, C.; Stranks, S. D., Controlling the Growth Kinetics and Optoelectronic Properties of 2D/3D Lead-Tin Perovskite Heterojunctions. *Adv. Mater.* 2019, 31, 1905247.
- (19) Ke, W.; Chen, C.; Spanopoulos, I.; Mao, L.; Hadar, I.; Li, X.; Hoffman, J. M.; Song, Z.; Yan, Y.; Kanatzidis, M. G., Narrow-Bandgap Mixed Lead/Tin-Based 2D Dion-Jacobson Perovskites Boost the Performance of Solar Cells. *J. Am. Chem. Soc.* 2020, 142, 15049-15057.
- (20) Tsai, H.; Nie, W.; Blancon, J.-C.; Stoumpos, C. C.; Asadpour, R.; Harutyunyan, B.; Neukirch, A. J.; Verduzco, R.; Crochet, J. J.; Tretiak, S., High-Efficiency Two-Dimensional Ruddlesden-Popper Perovskite Solar Cells. *Nature* 2016, 536, 312-316.
- (21) Gu, F.; Ye, S.; Zhao, Z.; Rao, H.; Liu, Z.; Bian, Z.; Huang, C., Improving Performance of Lead-Free Formamidinium Tin Triiodide Perovskite Solar Cells by Tin Source Purification. *Solar RRL* 2018, 2, 1800136.
- (22) Lin, R.; Xiao, K.; Qin, Z.; Han, Q.; Zhang, C.; Wei, M.; Saidaminov, M. I.; Gao, Y.; Xu, J.; Xiao, M., Monolithic All-Perovskite Tandem Solar Cells with 24.8% Efficiency Exploiting Comproportionation to Suppress Sn (II) Oxidation in Precursor Ink. *Nature Energy* 2019, 4, 864-873.

- (23) Jiang, T.; Chen, Z.; Chen, X.; Liu, T.; Chen, X.; Sha, W. E.; Zhu, H.; Yang, Y., Realizing High Efficiency over 20% of Low-Bandgap Pb-Sn-Alloyed Perovskite Solar Cells by In Situ Reduction of Sn<sup>4+</sup>. *Solar RRL* 2020, 4, 1900467.
- (24) He, X.; Wu, T.; Liu, X.; Wang, Y.; Meng, X.; Wu, J.; Noda, T.; Yang, X.; Moritomo, Y.; Segawa, H., Highly efficient tin Perovskite Solar Cells Achieved in A Wide Oxygen Concentration Range. *J. Mater. Chem. A* 2020, 8, 2760-2768.
- (25) Tai, Q.; Guo, X.; Tang, G.; You, P.; Ng, T. W.; Shen, D.; Cao, J.; Liu, C. K.; Wang, N.; Zhu, Y., Antioxidant Grain Passivation for Air-Stable Tin-Based Perovskite Solar Cells. *Angew. Chem. Int. Ed.* 2019, 58, 806-810.
- (26) Wang, T.; Tai, Q.; Guo, X.; Cao, J.; Liu, C.-K.; Wang, N.; Shen, D.; Zhu, Y.; Lee, C.-S.; Yan, F., Highly Air-Stable Tin-Based Perovskite Solar Cells through Grain-Surface Protection by Gallic Acid. *ACS Energy Lett.* 2020, 5, 1741-1749.
- (27) Gao, C.; Jiang, Y.; Sun, C.; Han, J.; He, T.; Huang, Y.; Yao, K.; Han, M.; Wang, X.; Wang, Y., Multifunctional Naphthol Sulfonic Salt Incorporated in lead-Free 2D Tin Halide Perovskite for Red Light-Emitting Diodes. *ACS Photonics* 2020, 7, 1915-1922.
- (28) Ma, C.; Park, N.-G., Paradoxical Approach with a Hydrophilic Passivation Layer for Moisture-Stable, 23% Efficient Perovskite Solar Cells. *ACS Energy Lett.* 2020, 5, 3268-3275.
- (29) Cheng, B.; Li, T.-Y.; Wei, P.-C.; Yin, J.; Ho, K.-T.; Retamal, J. R. D.; Mohammed, O. F.; He, J.-H., Layer-Edge Device of Two-Dimensional Hybrid Perovskites. *Nat Commun.* 2018, 9, 1-7.

- (30) Meng, X.; Wang, Y.; Lin, J.; Liu, X.; He, X.; Barbaud, J.; Wu, T.; Noda, T.; Yang, X.; Han, L., Surface-Controlled Oriented Growth of FASnI<sub>3</sub> Crystals for Efficient Lead-Free Perovskite Solar Cells. *Joule* 2020, 4, 902-912.
- (31) Weidman, M. C.; Seitz, M.; Stranks, S. D.; Tisdale, W. A., Highly Tunable Colloidal Perovskite Nanoplatelets through Variable Cation, Metal, and Halide Composition. *ACS Nano* 2016, 10, 7830-7839.
- (32) Kim, H.; Pei, M.; Lee, Y.; Sutanto, A. A.; Paek, S.; Queloz, V. I.; Huckaba, A. J.; Cho, K. T.; Yun, H. J.; Yang, H., Self-Crystallized Multifunctional 2D Perovskite for Efficient and Stable Perovskite Solar Cells. *Adv. Funct. Mater.* 2020, 30, 1910620.
- (33) Cao, D. H.; Stoumpos, C. C.; Farha, O. K.; Hupp, J. T.; Kanatzidis, M. G., 2D Homologous Perovskites as light-Absorbing Materials for Solar Cell Applications. *J. Am. Chem. Soc.* 2015, 137, 7843-7850.
- (34) Proppe, A. H.; Wei, M.; Chen, B.; Quintero-Bermudez, R.; Kelley, S. O.; Sargent, E. H., Photochemically Cross-Linked Quantum Well Ligands for 2D/3D Perovskite Photovoltaics with Improved Photovoltage and Stability. *J. Am. Chem. Soc.* 2019, 141, 14180-14189.
- (35) Zhou, X.; Zhang, L.; Wang, X.; Liu, C.; Chen, S.; Zhang, M.; Li, X.; Yi, W.; Xu, B., Highly Efficient and Stable GABr-Modified Ideal-Bandgap (1.35 eV) Sn/Pb Perovskite Solar Cells Achieve 20.63% Efficiency with a Record Small Voc Deficit of 0.33 V. *Adv. Mater.* 2020, 32, 1908107.

- (36) Yin, W.-J.; Shi, T.; Yan, Y., Unusual Defect Physics in CH<sub>3</sub>NH<sub>3</sub>PbI<sub>3</sub> Perovskite Solar Cell Absorber. *Appl. Phys. Lett.* 2014, 104, 063903.
- (37) Luo, D.; Su, R.; Zhang, W.; Gong, Q.; Zhu, R., Minimizing Non-Radiative Recombination Losses in Perovskite Solar Cells. *Nature Rev. Mater.* 2020, 5, 44-60.
- (38) Shao, Y.; Xiao, Z.; Bi, C.; Yuan, Y.; Huang, J., Origin and Elimination of Photocurrent Hysteresis by Fullerene Passivation in CH<sub>3</sub>NH<sub>3</sub>PbI<sub>3</sub> Planar Heterojunction Solar Cells. *Nat. Commun.* 2014, 5, 1-7.
- (39) Zheng, X.; Chen, B.; Dai, J.; Fang, Y.; Bai, Y.; Lin, Y.; Wei, H.; Zeng, X. C.; Huang, J., Defect Passivation in Hybrid Perovskite Solar Cells Using Quaternary Ammonium Halide Anions and Cations. *Nature Energy* 2017, 2, 1-9.
- (40) Chen, J.; Park, N. G., Causes and Solutions of Recombination in Perovskite Solar Cells. *Adv. Mater.* 2019, 31, 1803019.
- (41) Lin, Z.; Liu, C.; Liu, G.; Yang, J.; Duan, X.; Tan, L.; Chen, Y., Preparation of Efficient Inverted Tin-Based Perovskite Solar Cells via the Bidentate Coordination Effect of 8-hydroxyquinoline. *Chem. Commun.* 2020, 56, 4007-4010.
- (42) Wang, G.; Wang, C.; Gao, Y.; Wen, S.; MacKenzie, R. C.; Guo, L.; Dong, W.; Ruan, S., Passivation Agent with Dipole Moment for Surface Modification Towards Efficient and Stable Perovskite Solar Cells. *J. Energy Chem.* 2022, 64, 55-61.

- (43) Su, H.; Zhang, J.; Hu, Y.; Du, X.; Yang, Y.; You, J.; Gao, L.; Liu, S., Fluoroethylamine Engineering for Effective Passivation to Attain 23.4% Efficiency Perovskite Solar Cells with Superior Stability. *Adv. Energy Mater.* 2021, 11, 2101454.
- (44) Min, J.; Luponosov, Y. N.; Gasparini, N.; Richter, M.; Bakirov, A. V.; Shcherbina, M. A.; Chvalun, S. N.; Grodd, L.; Grigorian, S.; Ameri, T.; Ponomarenko, S. A.; Brabec, C. J., Effects of Alkyl Terminal Chains on Morphology, Charge Generation, Transport, and Recombination Mechanisms in Solution-Processed Small Molecule Bulk Heterojunction Solar Cells. *Adv. Energy Mater.* 2015, 5, 1500386.
- (45) Chen, Y.; Li, N.; Wang, L.; Li, L.; Xu, Z.; Jiao, H.; Liu, P.; Zhu, C.; Zai, H.; Sun, M., Impacts of Alkaline on the Defects Property and Crystallization Kinetics in Perovskite Solar Cells. *Nat Commun.* 2019, 10, 1-10.
- (46) Xu, G.; Xue, R.; Chen, W.; Zhang, J.; Zhang, M.; Chen, H.; Cui, C.; Li, H.; Li, Y.; Li, Y., New Strategy for Two-Step Sequential Deposition: Incorporation of Hydrophilic Fullerene in Second Precursor for High-Performance p-i-n Planar Perovskite Solar Cells. *Adv. Energy Mater.* 2018, 8, 1703054.
- (47) Zheng, X.; Hou, Y.; Bao, C.; Yin, J.; Yuan, F.; Huang, Z.; Song, K.; Liu, J.; Troughton, J.; Gasparini, N., Managing Grains and Interfaces via Ligand Anchoring Enables 22.3%-efficiency Inverted Perovskite Solar Cells. *Nature Energy* 2020, 5, 131-140.
- (48) Cowan, S. R.; Roy, A.; Heeger, A. J., Recombination in Polymer-Fullerene Bulk Heterojunction Solar Cells. *Phys. Rev. B* 2010, 82, 245207.

- (49) Wetzelaer, G. J. A.; Scheepers, M.; Sempere, A. M.; Momblona, C.; Ávila, J.; Bolink, H. J., Trap-assisted Non-Radiative Recombination in Organic-Inorganic Perovskite Solar Cells. *Adv. Mater.* 2015, 27, 1837-1841.
- (50) Erwin, W. R.; MacKenzie, R. C.; Bardhan, R., Understanding the Limits of Plasmonic Enhancement in Organic Photovoltaics. *J. Phys. Chem. C* 2018, 122, 7859-7866.
- (51) Majeed, N.; Saladina, M.; Krompiec, M.; Greedy, S.; Deibel, C.; MacKenzie, R. C., Using Deep Machine Learning to Understand the Physical Performance Bottlenecks in Novel Thin-Film Solar Cells. *Adv. Funct. Mater.* 2020, 30, 1907259.
- (52) Röhr, J. A.; MacKenzie, R. C., Analytical Description of Mixed Ohmic and Space-Charge-Limited Conduction in Single-Carrier Devices. *J. Appl. Phys.* 2020, 128, 165701.